

A generalized transport-velocity formulation for smoothed particle hydrodynamics

Chi Zhang, Xiangyu Y. Hu*, Nikolaus A. Adams

Lehrstuhl für Aerodynamik und Strömungsmechanik, Technische Universität München, 85748 Garching, Germany

ARTICLE INFO

Article history:

Received 19 May 2015

Received in revised form 21 November 2016

Accepted 6 February 2017

Available online 21 February 2017

Keywords:

Weakly-compressible SPH

Transport-velocity formulation

Tensile instability

ABSTRACT

The standard smoothed particle hydrodynamics (SPH) method suffers from tensile instability. In fluid-dynamics simulations this instability leads to particle clumping and void regions when negative pressure occurs. In solid-dynamics simulations, it results in unphysical structure fragmentation. In this work the transport-velocity formulation of Adami et al. (2013) [14] is generalized for providing a solution of this long-standing problem. Other than imposing a global background pressure, a variable background pressure is used to modify the particle transport velocity and eliminate the tensile instability completely. Furthermore, such a modification is localized by defining a shortened smoothing length. The generalized formulation is suitable for fluid and solid materials with and without free surfaces. The results of extensive numerical tests on both fluid and solid dynamics problems indicate that the new method provides a unified approach for multi-physics SPH simulations.

© 2017 Elsevier Inc. All rights reserved.

1. Introduction

As a fully Lagrangian, mesh-less method, smoothed particle hydrodynamics (SPH) was proposed by Lucy [1], Gingold and Monaghan [2] independently. SPH was originally developed for simulating astrophysical problems and has been applied successfully to a wide range of solid and fluid dynamic problems. For the simulation of solid dynamics SPH offers significant advantages in terms of handling large deformations in a purely Lagrangian frame. SPH uses a kernel function to approximate field quantities at arbitrarily distributed Lagrangian discretization elements (particles) in the form of particle interactions. For example, the particles repel or attract each other under the action of compression or tension, respectively. Subjected to tension, the mutual attraction of particles may result in a so-called tensile instability which can lead to unphysical fractures [3]. For the simulation of fluid dynamics tensile instability occurs when the static pressure becomes negative and results in particle clumping or void regions.

Several attempts have been carried out to address this problem since its first observation. Schüssler and Schmitt [4] proposed a new kernel function which can produce a repulsive force when negative pressure occurs. However, this function does not satisfy the requirement of continuous first-order derivatives. Jonson and Beissel [5] used a modified non-zero quadratic kernel function to reduce this instability. The problem of this kernel is that it does not have a continuous second-order derivative. Randles and Libersky [6] used a conservative smoothing approach to add stabilizing dissipation for removing the tensile instability. Mandell et al. [7] commented that this approach is good in some cases but only qualitatively correct in other cases. Dilts [8] proposed a moving-least-square particle hydrodynamics (MLSPH) method which

* Corresponding author.

E-mail address: xiangyu.hu@tum.de (X.Y. Hu).

replaces the SPH approximation with moving-least-square formulation to reduce tensile instability. While MLSPH is not locally conservative, it increases substantially computational cost compared with standard SPH. Dyka et al. [9] developed a stress-point algorithm which uses stress points located in the mid-way between particles to calculate the stress and maps it to SPH particles. Randles and Libersky [10] showed that this algorithm is stable but complex and computationally inefficient. Since SPH is a particle-based numerical method, a straightforward concept is to eliminate tensile instability by mimicking atomic forces rather than changing the kernel function [11]. Monaghan [12] and Gray et al. [11] developed an artificial stress algorithm to prevent particle clumping and successfully simulated the cases of an oscillating plate and colliding rubber rings. However, as pointed out by Lobovsky and Kren [13], this algorithm fails when the material has comparably high Poisson ratio.

Adami et al. [14] proposed a transport-velocity formulation to address particle clumping and void-region problems in weakly-compressible SPH simulation of flow at high Reynolds number. With the original transport-velocity formulation [14], the momentum equation is reformulated by moving particles with a transport velocity [15,16]. Using a globally constant background pressure for regulation, the transport velocity leads to favorable particle distribution and reduces numerical error [17]. A problem of the original transport-velocity formulation is that there is no straightforward applicability to problems with free fluid or solid material surfaces. This is due to the fact that a constant correcting background pressure may introduce a large artificial velocity at such boundaries. We emphasize that the idea of moving particles with a transport velocity which may differ from the momentum velocity was first proposed with the XSPH scheme to prevent penetration in impact problems [18]. Hu and Adams [15] utilized the transport velocity obtained from an intermediate projection step to impose fluid incompressibility. Xu et al. [19] developed a shifting approach in the incompressible SPH method for homogenized particle distribution. Lind et al. [20] extended this approach to simulate free surface flow with a surface-identification algorithm. Very recently, Vacondio et al. [21] modified this approach for a variable-resolution SPH method. Monaghan [22] developed an SPH turbulence model in which the used smoothed transport velocity can be related to the Lagrangian averaged Navier Stokes equations (LANS) [23]. However, none of these approaches was used to address the tensile-instability issue in SPH simulation of solid dynamics to the best knowledge of the authors.

In this paper, we extend the original transport-velocity formulation to solve the tensile instability problem of SPH for solid and fluid dynamic problems. Instead of a globally constant background pressure the present method uses a variable background pressure for the transport velocity correction. According to this modification the correction is proportional to the local pressure and can be implemented to problems with free fluid or solid material surfaces. Additionally, due to a shortened smoothing length, the background pressure correction is localized by involving only nearest-neighbor particles. The numerical results show that the present method eliminates the tensile instability completely in simulations of both solid and fluid dynamics. The remainder of this paper is arranged as follows: in the Section 2 and 3, the details of the method are described. A wide range of classical problems is tested in Section 4 and brief concluding remarks are given in Section 5.

2. Governing equations

The governing equations for continuum mechanics in a Lagrangian reference frame include the equations for conservation for mass and momentum. The mass-conservation equation is

$$\frac{d\rho}{dt} = -\rho \nabla \cdot \mathbf{v} \quad (1)$$

and the momentum-conservation equation is

$$\frac{d\mathbf{v}}{dt} = \frac{1}{\rho} \nabla \cdot \boldsymbol{\sigma} + \mathbf{g} \quad (2)$$

Here, ρ is density, \mathbf{v} is velocity, t is time, \mathbf{g} is the body force, $\boldsymbol{\sigma}$ is the stress tensor and

$$\frac{d(\bullet)}{dt} = \frac{\partial(\bullet)}{\partial t} + \mathbf{v} \cdot \nabla(\bullet) \quad (3)$$

refers to the material derivative. Note that Eqs. (1) and (2) allow a common description of both fluid and solid dynamics.

For elastic solid materials, the stress tensor $\boldsymbol{\sigma}$ can be decomposed into isotropic and deviatoric parts

$$\boldsymbol{\sigma} = -p\mathbf{I} + \boldsymbol{\sigma}', \quad (4)$$

where p is the hydrostatic pressure, \mathbf{I} is identity matrix and $\boldsymbol{\sigma}'$ is the deviatoric stress. Using Jaumann's formulation of the Hooke's law, the rate of change of the deviatoric stress can be described as

$$\frac{d\boldsymbol{\sigma}'}{dt} = 2G(\boldsymbol{\epsilon} - \frac{1}{3} \text{Tr}(\boldsymbol{\epsilon})\mathbf{I}) + \boldsymbol{\sigma}' \cdot \boldsymbol{\Omega}^T + \boldsymbol{\Omega} \cdot \boldsymbol{\sigma}', \quad (5)$$

where G is the shear modulus, $\boldsymbol{\epsilon}$ is the strain tensor

$$\boldsymbol{\epsilon} = \frac{1}{2} \left(\nabla \otimes \mathbf{v} + (\nabla \otimes \mathbf{v})^T \right), \quad (6)$$

and $\boldsymbol{\Omega}$ is the rotation tensor

$$\boldsymbol{\Omega} = \frac{1}{2} \left(\nabla \otimes \mathbf{v} - (\nabla \otimes \mathbf{v})^T \right). \quad (7)$$

For a weakly-compressible or incompressible fluid, the deviatoric stress vanishes and a viscous force is added to the stress tensor:

$$\boldsymbol{\sigma} = -p\mathbf{I} + 2\eta\boldsymbol{\epsilon}, \quad (8)$$

where η is the dynamic viscosity.

3. Numerical method

With the transport-velocity formulation [14] the momentum velocity for particle transport is modified, and we can redefine the material derivative of a particle moving with the transport velocity $\tilde{\mathbf{v}}$ as

$$\frac{\tilde{d}(\bullet)}{dt} = \frac{\partial(\bullet)}{\partial t} + \tilde{\mathbf{v}} \cdot \nabla(\bullet). \quad (9)$$

The mass-conservation equation for a Lagrangian particle is modified accordingly to

$$\frac{\tilde{d}\rho}{dt} = -\rho \nabla \cdot \tilde{\mathbf{v}} \quad (10)$$

and the momentum equation to

$$\frac{\tilde{d}\mathbf{v}}{dt} = \frac{1}{\rho} \nabla \cdot \boldsymbol{\sigma} + \frac{1}{\rho} \nabla \cdot \mathbf{A} + \mathbf{g}, \quad (11)$$

where the extra stress tensor $\mathbf{A} = \rho \mathbf{v} \otimes (\tilde{\mathbf{v}} - \mathbf{v})$ is a consequence of the modified transport velocity.

3.1. Evolution of density

Following the standard SPH method, the density evolution equation is discretized as

$$\frac{\tilde{d}\rho_a}{dt} = \rho_a \sum_b \frac{m_b}{\rho_b} \frac{\partial W_{ab}}{\partial r_{ab}} \mathbf{e}_{ab} \cdot \tilde{\mathbf{v}}_{ab}, \quad (12)$$

where m is the particle mass, $\tilde{\mathbf{v}}_{ab} = \tilde{\mathbf{v}}_a - \tilde{\mathbf{v}}_b$ is the relative transport velocity between particles a and b , $\frac{\partial W_{ab}}{\partial r_{ab}} \mathbf{e}_{ab}$ is gradient of the kernel function $W(\mathbf{r}_{ab}, h)$. Here, h is the smoothing length, $\mathbf{r}_{ab} = \mathbf{r}_a - \mathbf{r}_b = r_{ab} \mathbf{e}_{ab}$ and \mathbf{e}_{ab} is a normalized vector pointing from particle b to particle a . Note that when density evolution equation is applied for the simulation of weakly-compressible or incompressible fluid dynamics, it may lead to large density errors when the Reynolds number of the flow is large [24]. Therefore, similarly to Colagrossi and Landrini [24], the density field in fluid-dynamics simulation is reinitialized at each time-step by

$$\rho_a = \frac{\sum_b m_b W_{ab}}{\min(1, \sum_b W_{ab} \frac{m_b}{\rho^*})}, \quad (13)$$

where ρ^* is the density before reinitialization. Note that, limiting of the denominator is due to the fact that $\sum_b W_{ab} \frac{m_b}{\rho^*} \approx \int W(\mathbf{r} - \mathbf{r}_a, h) d\mathbf{r} \leq 1$, e.g. when a free surface passes through the support of $W(\mathbf{r} - \mathbf{r}_a, h)$. To calculate the divergence of deviatoric stresses of elastic solid dynamics, the velocity gradient can be approximated as

$$\left(\nabla \otimes \tilde{\mathbf{v}} \right)_a = \sum_b \frac{m_b}{\rho_b} \frac{\partial W_{ab}}{\partial r_{ab}} \tilde{\mathbf{v}}_{ab} \otimes \mathbf{e}_{ab} \quad (14)$$

3.2. Momentum equation

The momentum-conservation equation for an elastic solid material can be written as [25,26]

$$\frac{\tilde{d}\mathbf{v}_a}{dt} = - \sum_b m_b \frac{\partial W_{ab}}{\partial r_{ab}} \mathbf{e}_{ab} \cdot \left[\left(\frac{p_a}{\rho_a^2} + \frac{p_b}{\rho_b^2} \right) \mathbf{I} - \left(\frac{\boldsymbol{\sigma}'_a}{\rho_a^2} + \frac{\boldsymbol{\sigma}'_b}{\rho_b^2} \right) \right] + \mathbf{g}_a. \quad (15)$$

For fluid particles, the viscous force is obtained from the inter-particle-averaged shear viscosity in SPH form [27,15]

$$\eta_{ab} = \frac{2\eta_a \eta_b}{\eta_a + \eta_b}. \quad (16)$$

The discretized momentum-conservation equation for fluid particle is

$$\frac{\tilde{d}\mathbf{v}_a}{dt} = - \sum_b m_b \frac{\partial W_{ab}}{\partial r_{ab}} \mathbf{e}_{ab} \cdot \left[\left(\frac{p_a}{\rho_a^2} + \frac{p_b}{\rho_b^2} \right) \mathbf{I} - \left(\frac{\mathbf{A}_a}{\rho_a^2} + \frac{\mathbf{A}_b}{\rho_b^2} \right) \right] + \sum_b m_b \frac{\eta_{ab} \mathbf{v}_{ab}}{\rho_a \rho_b r_{ab}} \frac{\partial W_{ab}}{\partial r_{ab}} + \mathbf{g}_a. \quad (17)$$

The extra-stress term \mathbf{A} is not present in the momentum equation for solid dynamics as our numerical tests show that its influence is negligible due to the well resolved velocity field. This is consistent with the observation that, for flows up to moderate Reynolds numbers ($O(10^2)$), the influence of this term is negligible [16]. Actually, this correction term has notable influence only when the flow is at high Reynolds number [16] or is inviscid, see Sec. 4.7. Although the viscous term in Eq. (17) does not strictly conserve angular momentum, it is generally accurate even for rotational flow as shown in Refs. [27,15]. Similarly to the viscous force term the present form of the extra-stress term in Eq. (17) does not strictly conserve the angular momentum either. As will be shown in Sec. 4.5, the angular-momentum conservation errors generally are very small. Following the weakly-compressible SPH (WCSPH) approach [28,27], pressure is calculated from an artificial isothermal equation of state:

$$p = K \left(\frac{\rho}{\rho_0} - 1 \right), \quad (18)$$

where $K = \rho_0 c_0^2$ is the bulk modulus. Here, the constants c_0 and ρ_0 are the reference sound speed and density, respectively. Note that, since Eq. (18) gives zero pressure at reference density, negative pressure occurs when $\rho < \rho_0$.

3.3. Particle transport velocity

In Adami et al. [14], instead of the momentum velocity the transport velocity $\tilde{\mathbf{v}}$ is used for particle transport

$$\frac{d\mathbf{r}_a}{dt} = \tilde{\mathbf{v}}_a. \quad (19)$$

The transport velocity at every time step is obtained by modifying the momentum velocity, i.e.,

$$\tilde{\mathbf{v}}_a(t + \delta t) = \mathbf{v}_a(t) + \delta t \left(\frac{\tilde{d}\mathbf{v}_a}{dt} - \frac{1}{\rho_a} \nabla p^0 \right), \quad (20)$$

where the term $\frac{1}{\rho_a} \nabla p^0$ is discretized as

$$\frac{1}{\rho_a} \nabla p^0 = p^0 \sum_b m_b \left(\frac{1}{\rho_a^2} + \frac{1}{\rho_b^2} \right) \frac{\partial W_{ab}}{\partial r_{ab}} \mathbf{e}_{ab} = \left(\frac{d\mathbf{v}_a}{dt} \right)_c, \quad (21)$$

where p^0 in Adami et al. [14] is a globally constant background pressure whose exact gradient vanishes. In SPH, however, the conservative approximation of the gradient for constant background pressure results in a residual force due to the lack of zero-order consistency. This residual force leads to a self-relaxation mechanism which regularizes the particle distribution such that it assumes approximately a configuration with low consistency error [17].

If we consider the right-hand-side of Eq. (21) as a general correction of the particle acceleration such that $\left(\frac{d\mathbf{v}_a}{dt} \right)_c$ is proportional to p^0 , we are free to choose different p^0 for different particles, or a different influence radii of such a correction. In this paper, we propose to modify Eq. (21) as

$$\left(\frac{d\mathbf{v}_a}{dt} \right)_c = p_a^0 \sum_b m_b \frac{1}{\rho_a^2} \frac{\partial \tilde{W}_{ab}}{\partial r_{ab}} \mathbf{e}_{ab}, \quad (22)$$

where $\tilde{W}_{ab} = W(\mathbf{r}_{ab}, \tilde{h})$ and $\tilde{h} = 0.5h$, which indicates that only the nearest-neighbor particles within the distance $2\tilde{h}$ affect the correction. Here, p_a^0 is chosen as

$$p_a^0 = \min(10|p_a|, p_{ref}), \quad (23)$$

where p_{ref} is a reference pressure to avoid excessive time-step size limitation. For a weakly-compressible fluid or solid, a typical choice is $p_{ref} = K$. For compressible fluid or solid, $p_{ref} = \max(|p|_{\max}, K)$, where $|p|_{\max}$ is the maximum pressure magnitude in the entire domain. While Eq. (22) implies that the correction is proportional to the local particle pressure, it also implies that there is no, or only a very slight correction for a particle near a free fluid or solid material surface due to the surface boundary condition. Note that the factor of $|p_a|$ in Eq. (23) and the size of \tilde{h} in \tilde{W}_{ab} may affect the correction effectiveness. By preliminary numerical tests we found that the parameters of 10 and $0.5h$ are generally suitable. Therefore, we use the same values for all numerical tests of solid and fluid dynamics throughout this paper.

3.4. Time integration scheme

Similarly to Adami et al. [14], the kick-drift-kick scheme [29] is used for time integration. First the momentum velocity and transport velocity are calculated at the half time step,

$$\mathbf{v}_a^{n+\frac{1}{2}} = \mathbf{v}_a^n + \frac{\Delta t}{2} \left(\frac{\tilde{d}\mathbf{v}_a}{dt} \right)^n, \quad (24)$$

$$\tilde{\mathbf{v}}_a^{n+\frac{1}{2}} = \mathbf{v}_a^{n+\frac{1}{2}} + \frac{\Delta t}{2} \left(\frac{d\mathbf{v}_a}{dt} \right)_c^n. \quad (25)$$

Then the time derivatives of density and deviatoric stresses are calculated using the transport velocity by Eq. (12). The new time step density, deviatoric stresses and particle position are updated by

$$\rho_a^{n+1} = \rho_a^n + \Delta t \left(\frac{\tilde{d}\rho_a}{dt} \right)^{n+\frac{1}{2}}, \quad (26)$$

$$\boldsymbol{\sigma}'_a^{n+1} = \boldsymbol{\sigma}'_a^n + \Delta t \left(\frac{\tilde{d}\boldsymbol{\sigma}'_a}{dt} \right)^{n+\frac{1}{2}}, \quad (27)$$

$$\mathbf{r}_a^{n+1} = \mathbf{r}_a^n + \Delta t \tilde{\mathbf{v}}_a^{n+\frac{1}{2}}. \quad (28)$$

Finally, at new time-step particle position, the momentum velocity is updated

$$\mathbf{v}_a^{n+1} = \mathbf{v}_a^{n+\frac{1}{2}} + \frac{\Delta t}{2} \left(\frac{\tilde{d}\mathbf{v}_a}{dt} \right)^{n+1}. \quad (29)$$

For numerical stability several time step criteria should be satisfied, including the CFL condition

$$\Delta t \leq 0.25 \left(\frac{h}{c + |U|} \right), \quad (30)$$

where $|U|$ is the maximum velocity magnitude, the viscous condition

$$\Delta t \leq 0.25 \left(\frac{h^2}{\nu} \right), \quad (31)$$

and the body-force condition

$$\Delta t \leq 0.25 \sqrt{h/g}. \quad (32)$$

For solid dynamics, the elastic stress condition is

$$\Delta t \leq 0.25 \left(\frac{h}{\sqrt{\frac{E}{\rho_0}} + |U|} \right), \quad (33)$$

where E denotes the Young's modulus.

4. Numerical examples

A wide range of classical test problems, including free-surface flow, elastic-solid dynamics, high-velocity impact and Taylor-Green vortex flow, are studied. The Wendland C2 [30] kernel function and a constant smoothing length, $h = 1.3 \times \Delta x$, where Δx is the initial particle distance are used for all tests.

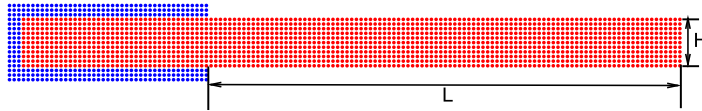


Fig. 1. Computational domain of the oscillating plate.

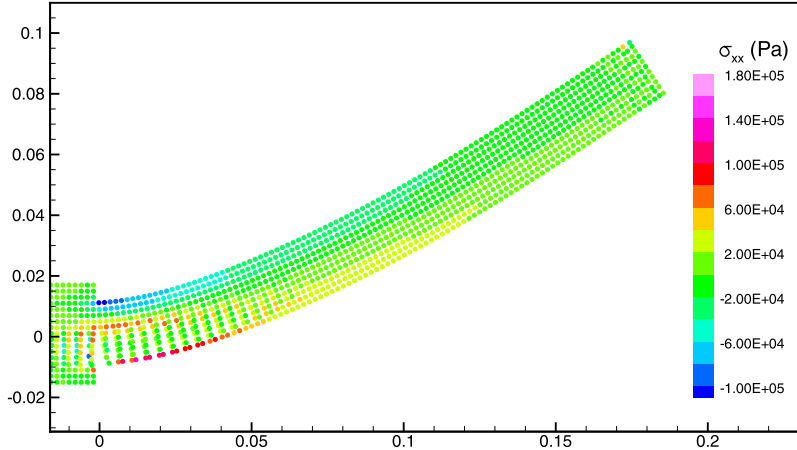


Fig. 2. Simulation of the oscillating plate using standard SPH method and particles are colored by σ_{xx} stress field ($L = 0.2$ m, $H = 0.02$ m and $V_f = 0.05$ m/s) at $t = 0.03$ s.

4.1. Oscillating plate

Landau and Lifshits [31] studied theoretically the oscillation of a thin plate with one edge fixed. Gray et al. [11] investigated the 2D model numerically using SPH method with artificial stresses for suppressing tensile instability. As shown in Fig. 1, the plate is clamped between layers of SPH particles which are not allowed to move and the motion of plate particles is initialized by a velocity profile, which is perpendicular to the plate and given by

$$v_y(x) = V_f c_0 \frac{F(x)}{F(L)}, \quad (34)$$

where, the constant of V_f varies for the different cases, L is the length of plate,

$$F(x) = (\cos kL + \cosh kL)(\cosh kx - \cos kx) + (\sin kL - \sinh kL)(\sinh kx - \sin kx), \quad (35)$$

where k is the wave number which can be derived from $kL = 1.875$. We set the plate properties as follows: Young's modulus $E = 2.0 \times 10^6$ Pa, density $\rho = 1000.0$ kg/m³ and Possion ratio $\nu = 0.3975$. In our simulation, the initial particle spacing is set as $\Delta x = 0.002$ m, and the reference sound speed $c_0 = \sqrt{\frac{E}{3(1-2\nu)\rho}}$. Because of the tensile instability of standard SPH unphysical fracture results, and the plate breaks where the maximum tensile stress appears, as shown in Fig. 2. With the present method the tensile instability is eliminated and the simulation is stable as shown in Fig. 3. A highly nonlinear case with large value of V_f is also simulated, as shown in Fig. 4. The results show that the simulation is stable even though the plate is strongly deformed. Note that these results are in good agreement with those obtained by the artificial stress algorithm in Gray et al. [11].

A convergence study and a comparison between numerical and analytical results are performed to demonstrate the accuracy of present method. For the convergence study, different resolutions are tested by varying initial particle spacing. The amplitude, as a function of time, of the mid-point in thickness direction at the end of plate is shown in Fig. 5. This study indicates that the period and amplitude of the oscillations converge rapidly with increasing resolution. The comparison of the first period of oscillations for a wide range of values of V_f obtained from numerical and analytical results is shown in the Table 1. The errors are around 13%, as the analytical results are based on a thin plate model, and in our simulation $H/L = 0.1$. Results of other cases at $H/L = 0.05$ are shown in the Table 2 and the errors decease to around 2.5% confirming previous numerical studies [11].

4.2. Colliding rubber rings

The collision of rubber rings was first investigated by Swegle et al. [3]. Our aim here is to show that, with the present method, the “numerical fracture” produced by the standard SPH the simulation does not occur. Monaghan [12] and Grey et al. [11] simulated this problem with artificial stresses to suppress tensile instability.

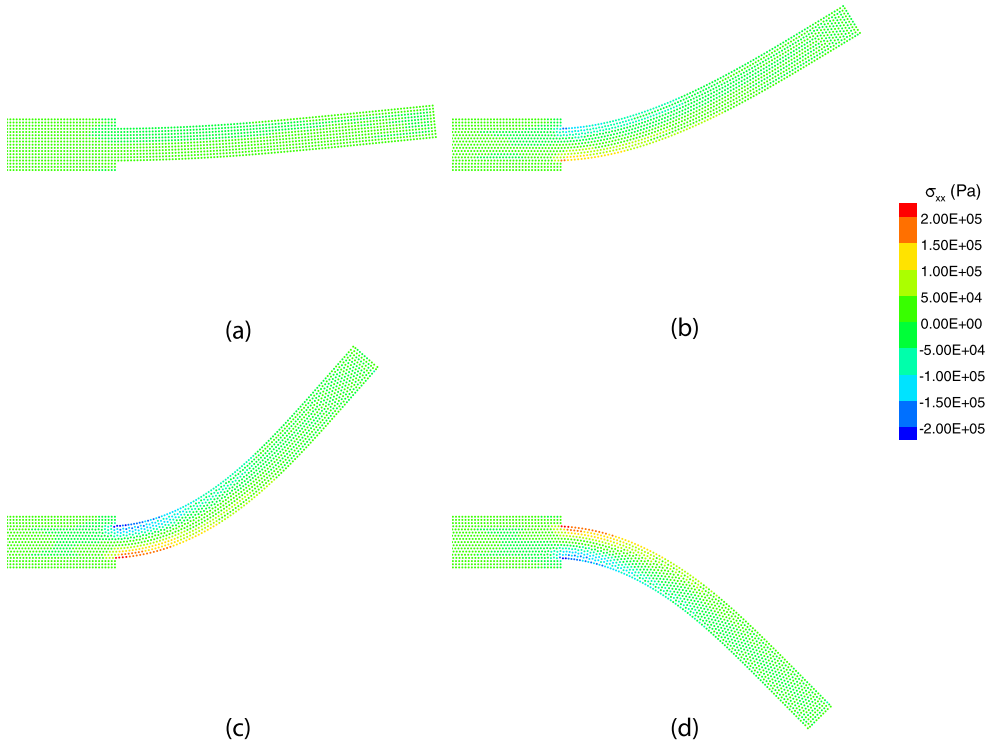


Fig. 3. Simulation of the oscillating plate using the present method and particles are colored by σ_{xx} stress field ($L = 0.2$ m, $H = 0.02$ m and $V_f = 0.05$ m/s): (a) $t = 0.01$ s, (b) $t = 0.05$ s, (c) $t = 0.07$ s, (d) $t = 0.22$ s.

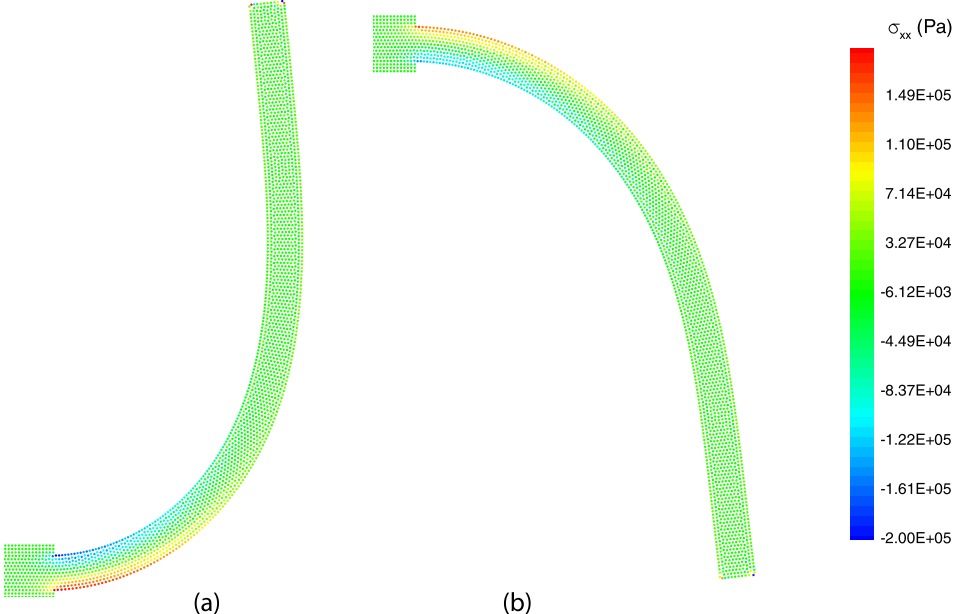


Fig. 4. Highly nonlinear case of an oscillating plate using the present method and particles are colored by σ_{xx} stress field ($L = 0.2$ m, $H = 0.01$ m and $V_f = 0.05$ m/s): (a) $t = 0.25$ s, (b) $t = 0.51$ s.

As shown in Fig. 6 (a) the inner ring radius is $r_{min} = 0.03$ m and the outer ring radius is $r_{max} = 0.04$ m. The rings have the same material properties: Young's modulus $E = 0.01$ GPa and density $\rho = 1.2 \times 10^3$ kg/m³. We set the rubber ring relative velocity as $v_0 = 0.12c_0$ and the initial particle spacing as $\Delta x = 0.001$ m.

The first test is with a Poisson ratio $\nu = 0.3975$. The results are shown in Fig. 6, which are in agreement with those of Grey et al. [11]. To show the improvement due to the present method, a case with $\nu = 0.447$ is also simulated. The results,

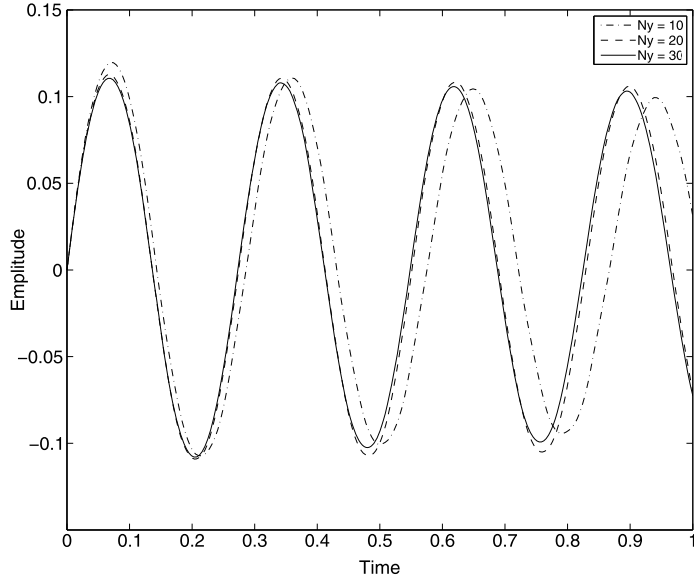


Fig. 5. Convergence study of the present method for the oscillating plate ($L = 0.2$ m, $H = 0.01$ m and $V_f = 0.05$ m/s).

Table 1

Comparison between analytical and numerical result for the first period of the oscillating plate at $L = 0.2$ m and $H = 0.02$ m for various V_f .

V_f	0.001	0.01	0.03	0.05
T_{SPH}	0.284	0.283	0.284	0.285
$T_{analytical}$	0.254	0.252	0.254	0.254

Table 2

Comparison between analytical and numerical result for the first period of the oscillating plate at $L = 0.2$ m and $H = 0.01$ m for various V_f .

V_f	0.001	0.01	0.03	0.05
T_{SPH}	0.521	0.520	0.522	0.520
$T_{analytical}$	0.508	0.508	0.508	0.508

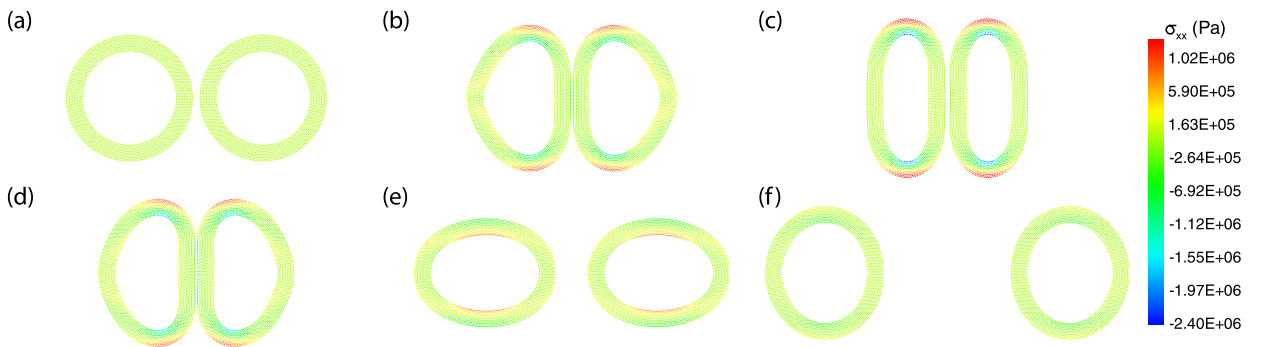


Fig. 6. Collision of rubber rings with $v = 0.3975$ using the present method and particles are colored by σ_{xx} stress field: (a) $t = 0.0$ s, (b) $t = 0.02$ s, (c) $t = 0.05$ s, (d) $t = 0.07$ s, (e) $t = 0.12$ s, (f) $t = 0.15$ s.

as shown in Fig. 7, exhibit no structure fragmentation. Note that Lobovsky and Kren [13] point out that the method of Grey et al. [11] produces “numerical fracture” for this case if the same parameters as for the case with $v = 0.3975$ are used.

Furthermore, a challenging case with Poisson ratio $\lambda = 0.49$, i.e. the value of real rubber, is simulated. The results, as shown in Fig. 8, indicate that no “numerical fracture” is produced. Note that, we have run this case with an even larger

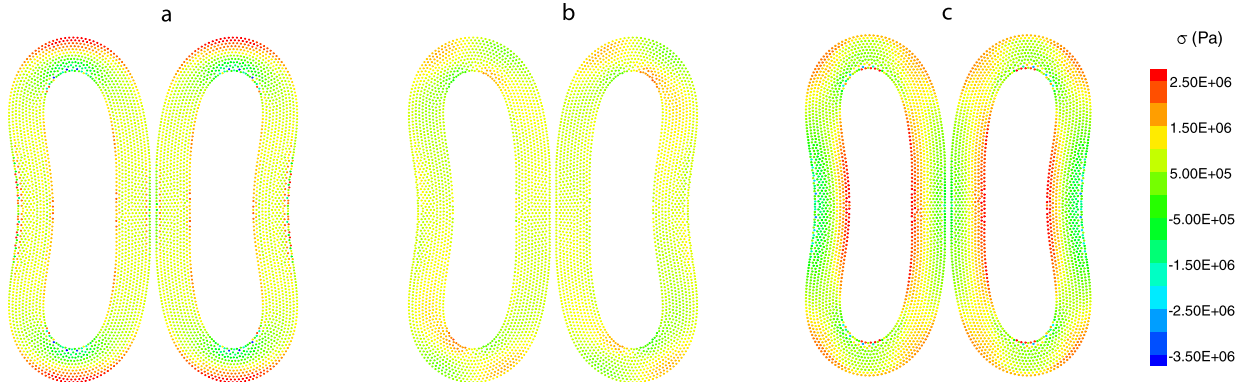


Fig. 7. Collision of rubber rings with $\nu = 0.47$ using the present method and stress field profile: (a) σ_{xx} , (b), σ_{xy} , (c) σ_{yy} .

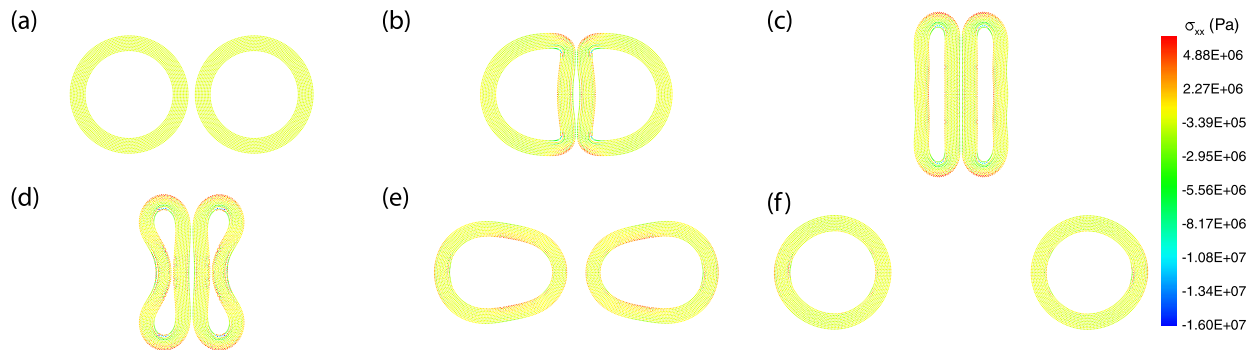


Fig. 8. Collision of rubber rings with $\nu = 0.49$ using the present method and particles are colored by σ_{xx} stress field: (a) $t = 0.0$ s, (b) $t = 0.03$ s, (c) $t = 0.12$ s, (d) $t = 0.19$ s, (e) $t = 0.25$ s, (f) $t = 0.34$ s.

Poisson ratio $\lambda = 0.499$ to demonstrate numerical stability. As the results do not exhibit visible difference from those at $\lambda = 0.49$ we refrain from showing them additionally.

4.3. Interaction involving realistic rubber material

Here, we consider another interesting problem, a low-velocity ball impact on a rubber target. Again, our aim here is to show that, with the present method, the “numerical fragmentation” does not occur. To simulate this problem in 2D, the ball is represented by a circular object with radius $r = 5$ mm and the target is modeled by a rubber filament with two ends fixed and has size of 2×50 mm, as shown in Fig. 9 (a). Ball and target have the same material property, Young’s modulus $E = 0.01$ GPa, density $\rho = 1.2 \times 10^3$ kg/m³ and Poisson ratio $\nu = 0.49$. In this simulation, the initial velocity of the ball is set as $v_0 = 0.15c_0$, and the initial particle spacing is $\Delta x = 0.5$ mm.

Fig. 9 shows the process of the impact. As expected, the target experiences a significant tensile deformation during the impact and then rebounds the ball as the elastic force increases. During the impact a wave propagating from the impact point can be observed and results in a bow-shaped deformation, as shown in Fig. 9 (b), (d). The simulation reproduces the complex impact dynamics, and tensile instability is completely eliminated. To our knowledge, this is the first successful SPH simulation of ball-target impact involving realistic rubber materials.

4.4. High-velocity impact (HVI)

High-velocity impact on a structure is a challenge for spacecraft design [32,33]. The HVI problem results in large deformation of structures [34,35], thus a robust and accurate numerical method is required for prediction.

Here, we consider a high-velocity aluminum projectile impacting on a thin target of the same material. The computational domain is shown in Fig. 10. The projectile is 10 mm in diameter, and the rectangular target has a size of 2×50 mm. The projectile and the target both have the following material properties: density $\rho = 2785$ kg/m³, sound speed $c_0 = 5328$ m/s, shear modulus $G = 2.76 \times 10^7$ kPa, yield modulus $Y_0 = 3.0 \times 10^5$ kPa. The impact velocity is set as $V_0 = 3100.0$ m/s. The initial particle spacing is $\Delta x = 0.5$ mm, and the simulation is started at the moment of impact. By using an elastic-perfectly plastic constitutive model [36,37], the deviatoric stress σ' in Eq. (10) is bounded by a factor

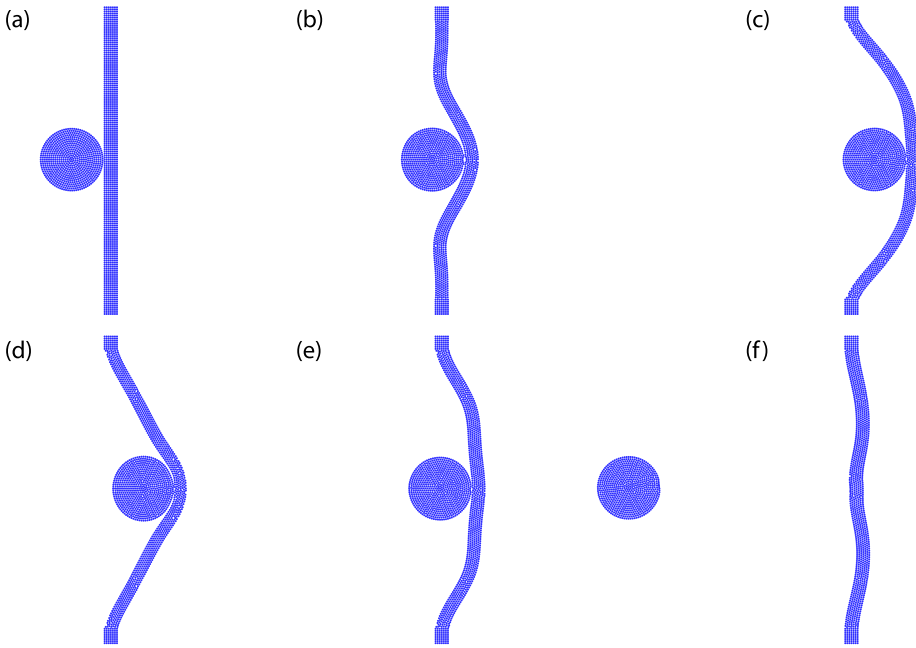


Fig. 9. Rubber projectile impact on target using the present method: (a) $t = 0.0$ ms, (b) $t = 0.33$ ms, (c) $t = 0.88$ ms, (d) $t = 1.20$ ms, (e) $t = 1.88$ ms, (f) $t = 4.08$ ms.

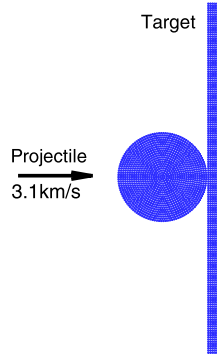


Fig. 10. Computational domain of the high velocity impact problem.

$\alpha = \min(\frac{v_0^2}{3J_2}, 1)$, where J_2 is calculated from $J_2 = \frac{1}{2}\sigma' : \sigma'$. As the pressure generated by the high-velocity impacting is much larger than the yield stress of aluminum, a highly localized plastic deformation is expected.

Fig. 11 shows the material geometry at several time instances after initial impact as predicted by the present method. As expected, the strong compression generated by the impact produces extreme pressures. A shock wave of about 1.0×10^7 kPa is observed to travel leftward to the projectile, closely followed by a rarefaction formed at the rear face of the target. As consequence, a large tensile force is produced. While the tensile force can lead to “numerical fracture” for the standard SPH method due to tensile instability [38,39] the present method does not produce such an artifact. Also note that, although using a much simpler material model, the target deformation is in qualitative agreement with previous SPH and free-Lagrangian simulations [38]. Furthermore, the progress of the projectile through the target, about 20.9 mm, and the width of the hole, about 19.8 mm, at $t = 8$ μ s are also close to those obtained by Ref. [38], as the evolution is dominated by inertial effects and much less effected by details of the material model [38].

4.5. Circular patch

We consider the evolution of a circular patch of an inviscid fluid with a nonuniform initial vorticity distribution. A very similar case has been studied by Antuono et al. [40]. The configuration is considered as a circular cylinder with radius $R = 1$ rotating with an angular velocity $\omega = \omega(r)$ as shown in Fig. 12 (a). The circular patch is subjected to a radial force given by $\mathbf{g} = -\beta^2 r \mathbf{r}$ where β is a constant parameter, r is the radial coordinate and \mathbf{r} is the radial unit vector. The initial profiles of angular velocity and pressure are given by

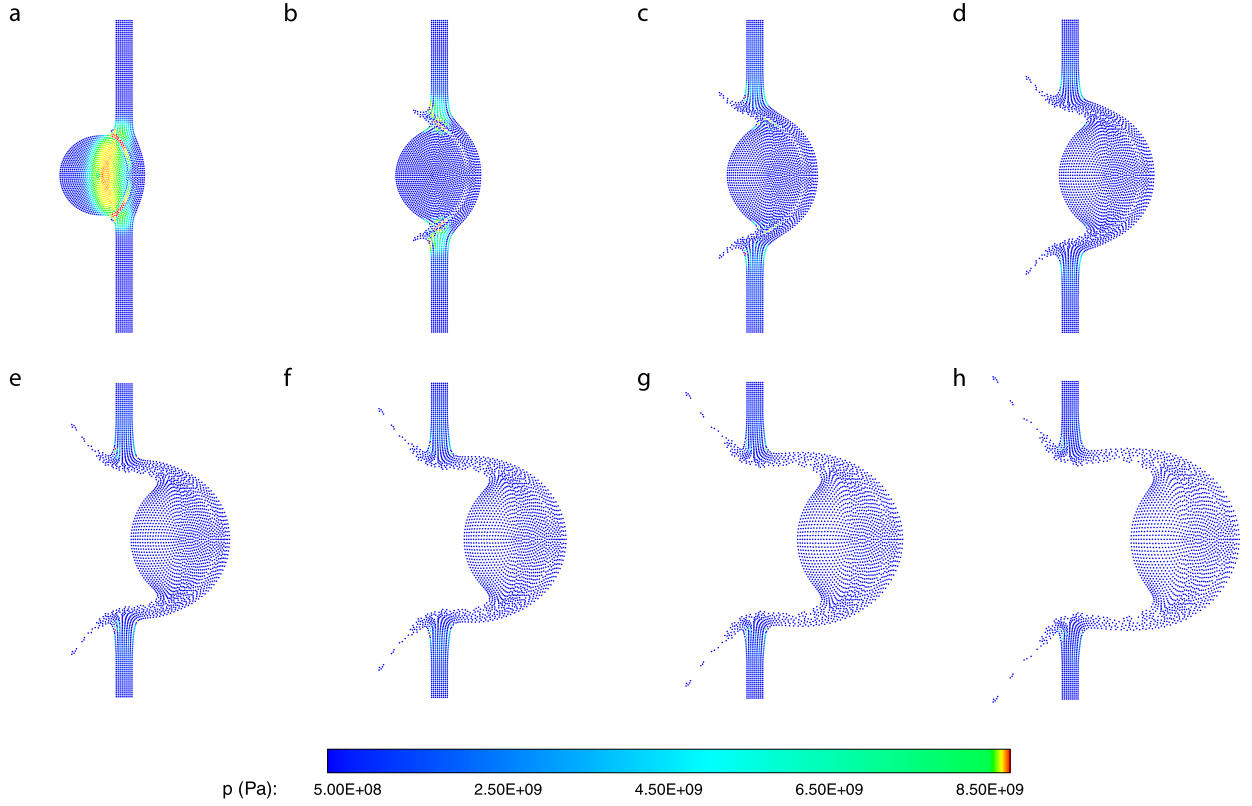


Fig. 11. Instantaneous results illustrating the deformation of structures in a HVI problem simulated by the present method: (a) $t = 1 \mu\text{s}$, (b) $t = 2 \mu\text{s}$, (c) $t = 3 \mu\text{s}$, (d) $t = 4 \mu\text{s}$, (e) $t = 5 \mu\text{s}$, (f) $t = 6 \mu\text{s}$, (g) $t = 7 \mu\text{s}$, (h) $t = 8 \mu\text{s}$.

$$\begin{cases} r\omega^2(r, 0) = \frac{1}{\rho_0} \frac{\partial p}{\partial r} + \beta^2 r \\ \omega(r, 0) = \omega_0 \left\{ \frac{l^2}{l^2+r^2} + 2 \frac{l^2 R}{(l^2+R^2)^2} r \right\}. \end{cases} \quad (36)$$

The constant parameters are $l^2 = 0.2 \text{ m}^2$, $\omega_0 = 1 \text{ s}^{-1}$ and $\beta = \frac{\pi}{8} \text{ s}^{-1}$, and the computational setup follows Ref. [40].

Fig. 12 shows the numerical results obtained with the present method and with standard SPH with and without artificial viscosity. While the present method and the standard SPH without artificial viscosity dissipate less kinetic energy, $\sum \frac{1}{2} v_i^2$, at the early times, the standard SPH with artificial viscosity dissipates less kinetic energy at longer times, as shown Fig. 12 (b). This may be related to the fact that artificial viscosity supports solid-body rotation behavior. The kinetic energy decays obtained by the present method with and without the extra-stress term \mathbf{A} , as shown in Fig. 12 (b), differ only slightly.

Fig. 12 (c) gives the evolution of the angular momentum obtained by different methods. Standard SPH with or without artificial viscosity conserves the angular momentum while the present method loses conservation because particles move with the transport velocity other than the momentum velocity. However, the conservation errors are very small as shown in Fig. 12 (c).

Fig. 12 (d) gives the evolution of circulation along the ring $r = 0.5$ and the circulation Γ is calculated through $\Gamma = 0.5 \sum \mathbf{v}_i \cdot (\mathbf{x}_{i+1} - \mathbf{x}_{i-1})$, where i denotes the label of a particle on the ring and \mathbf{x}_{i-1} , and \mathbf{x}_{i+1} represent the positions of the two nearest particles on the same ring. It is observed that the present method and the standard SPH with artificial viscosity conserve circulation better than the latter without artificial viscosity. None of the three methods conserves the circulation exactly. As particles move with the transport velocity in the present method one may rather approximate the circulation as $\Gamma_{tv} = 0.5 \sum \tilde{\mathbf{v}}_i \cdot (\mathbf{x}_{i+1} - \mathbf{x}_{i-1})$, which is damped considerably less compared with the circulation obtained by momentum velocity. Note that more demanding tests are also discussed in Antuono et al. [40], and further investigation of the circulation conservation of the present method with such tests is subject of future work.

4.6. Dam-break problem

The dam-break problem is taken from Ref. [41]. A liquid column of height $H = 1$ and length $L = 2H$ is located at the left side of a tank which has a length $l = 5.366H$ and height $h = 2H$. The liquid has a density $\rho = 1$ and the gravity is set as $g = 1$. A wall boundary condition proposed by Adami et al. [41] is implemented.

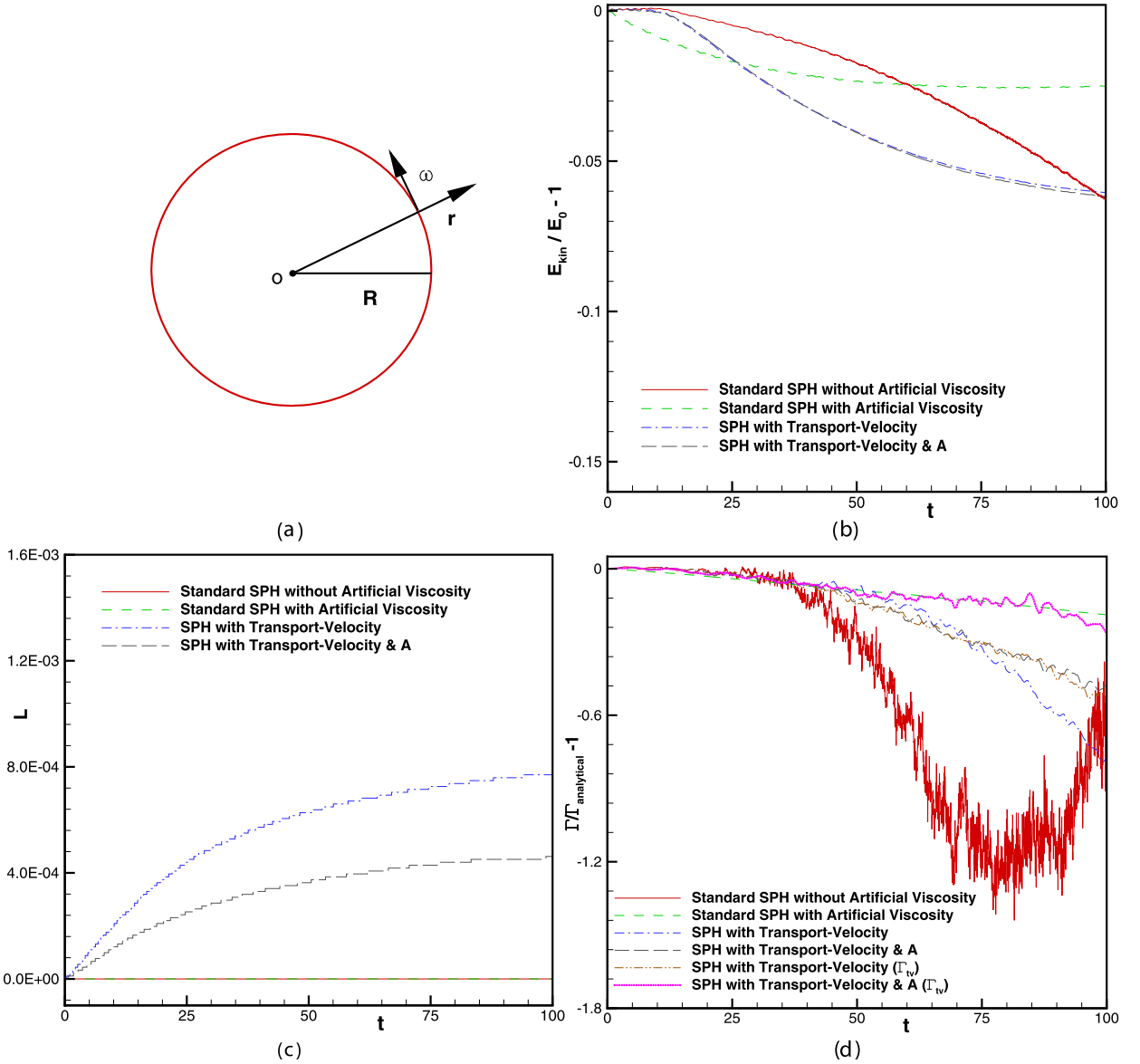


Fig. 12. Evolution of a circular patch of an inviscid fluid: (a) Configuration of circular patch; (b) Evolution of kinetic energy; (c) Evolution of angular momentum; (d) Evolution of circulation.

We consider the liquid as viscous and inviscid, respectively. For viscous flow the Reynolds number is set as $Re = \frac{U_{\max} H}{\nu} = 400$, where $U_{\max} = 2\sqrt{gH}$, reproducing the same case as in Adami et al. [41]. If the liquid is considered as inviscid this problem is very challenging, and the standard SPH requires artificial viscosity or diffusion to stabilize the simulation. The problem was simulated previously by Colagrossi and Landrini [24] with several stabilization approaches, such as moving-least-square density re-normalization, artificial viscosity and the XSPH method for transporting particles [18].

Fig. 13 (a) presents snapshots of the particle distribution and pressure profiles at different time instances for the viscous flow. Note that these results are in good agreement with those (their Fig. 14) of Adami et al. [41]. Quite similar run-up along the downstream wall after impact and reflected jet following the re-entry of backward wave can be observed in both simulations. Fig. 13 (b) shows the evolution of the particle distribution for the inviscid flow. The enlarged views of the fluid particles at $t = 6.2$, as shown in Fig. 14, suggest very regular pressure distribution is obtained by both viscous and inviscid simulations. It can be observed that the present results for the inviscid flow share several typical features with those in Ref. [24], such as a high run-up along the downstream wall, a large reflected jet and a large void in the downstream flow due to the re-entry of backward wave. A different feature obtained for the inviscid flow by the present method is the more intense splashing which agrees with experimental observations, such as in Lobovsky et al. [42] and other simulations such as that of Ferrari et al. [43].

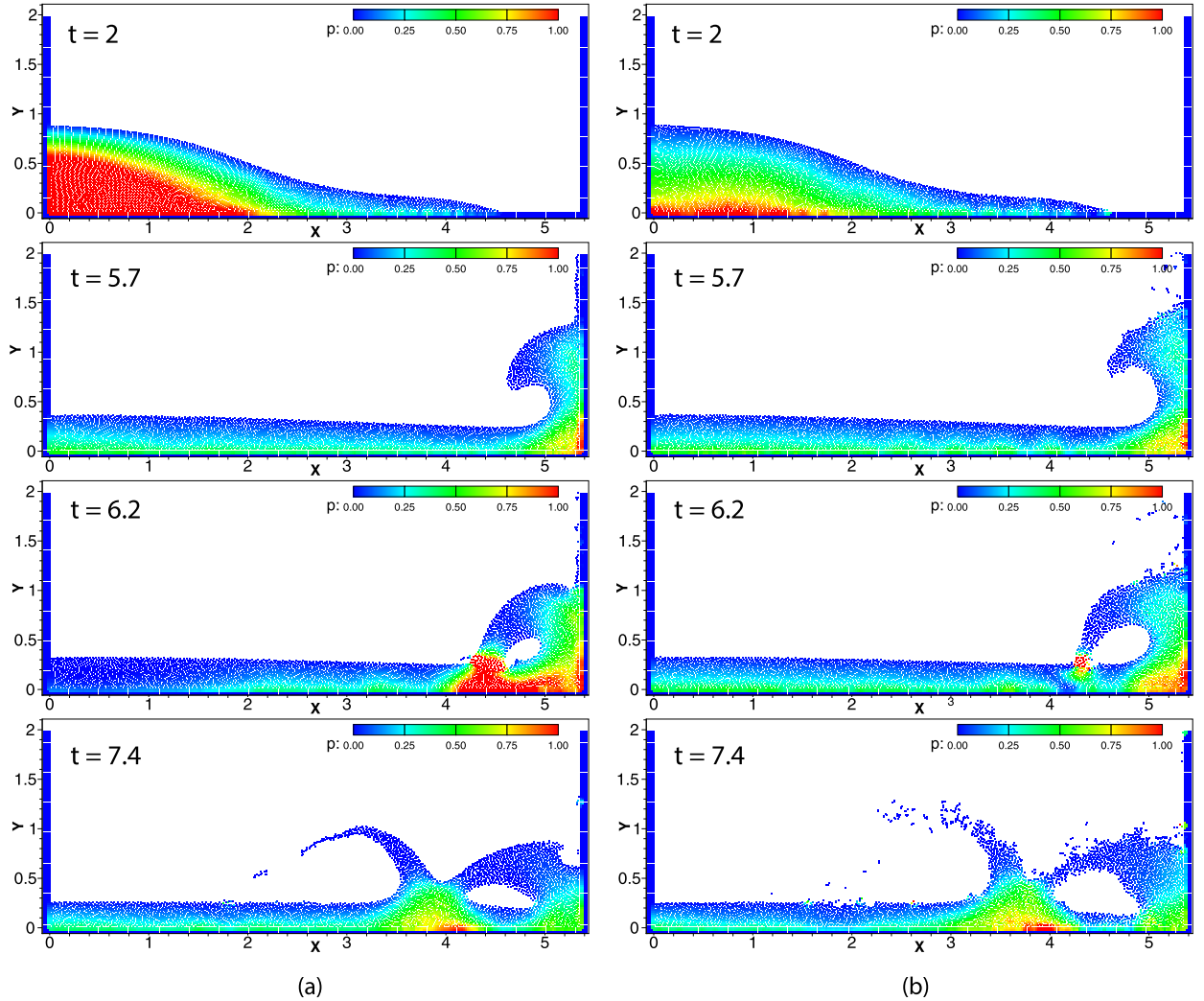


Fig. 13. Several snapshots of the particle distribution and pressure profile (colored by the pressure field) in the simulation of the dam-break problem with 5000 fluid particles: (a) Viscous flow solution; (b) Inviscid flow solution.

Fig. 15 (a) shows the water front location compared with experimental data [44,45] and theoretical result [46]. The inviscid solution, while overestimating the velocity of the liquid-front obtained from experiment, converges to the theoretical result. The viscous solution, similar to that of Adami et al. [41], achieves a better agreement with the experiment. We should point out that the present Reynolds number is much smaller than that (estimated as 5×10^5) in the experiment. **Fig. 15** (b) shows the pressure profile on the right wall at $y_0 = 0.2H$ obtained from both the inviscid and viscous solutions. Note that the probe position is the same as in Adami et al. [41] and Greco [47], not exact match the setup as in experiment. Similarly to Adami et al. [41] and Greco [47], the jump is well predicted and the numerical impact peak (around $t = 6.5$) is slightly delayed due to the fact that the air cushion is not considered here. Note that, compared with the viscous simulation, the inviscid simulation shows strong pressure fluctuations, e.g. spikes during the flow impact at the downstream wall.

4.7. Taylor-Green vortex

The 2D viscous Taylor-Green vortex flow has been simulated by SPH with the original transport-velocity formulation. As the standard SPH method leads to over-dissipation in simulation of Taylor-Green flow problems, and the original transport-velocity formulation solved this difficulty, we show that the present method recovers the original formulation for flows without free surface. Taylor-Green flow is a periodic array of vortices with the velocity of analytical solution given by

$$\begin{aligned} u(x, y, t) &= -Ue^{bt} \cos(2\pi x) \sin(2\pi y), \\ v(x, y, t) &= Ue^{bt} \sin(2\pi x) \cos(2\pi y), \end{aligned} \quad (37)$$

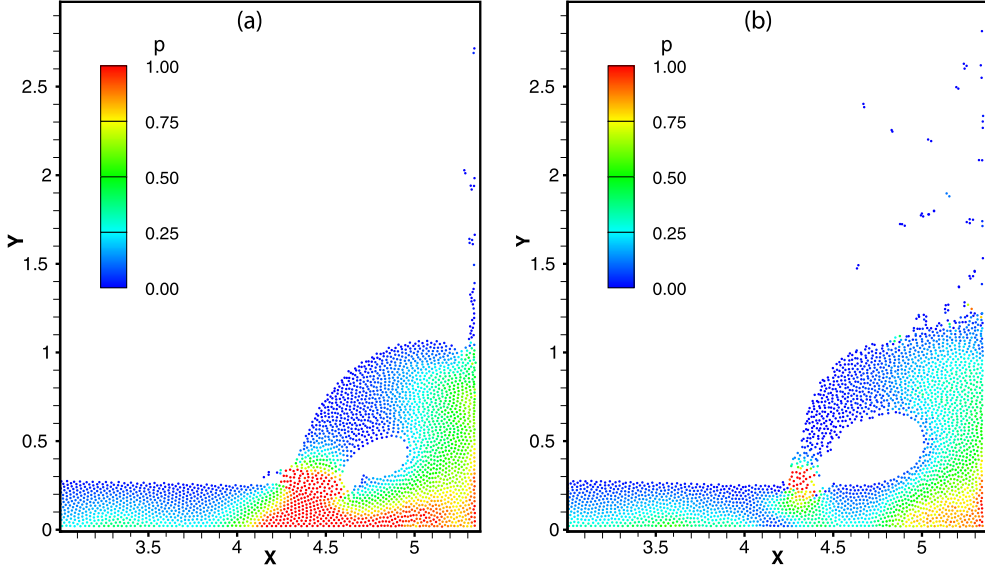


Fig. 14. Enlarged view of the impact of dam break flow at $t = 6.2$: (a) Viscous flow solution; (b) Inviscid flow solution.

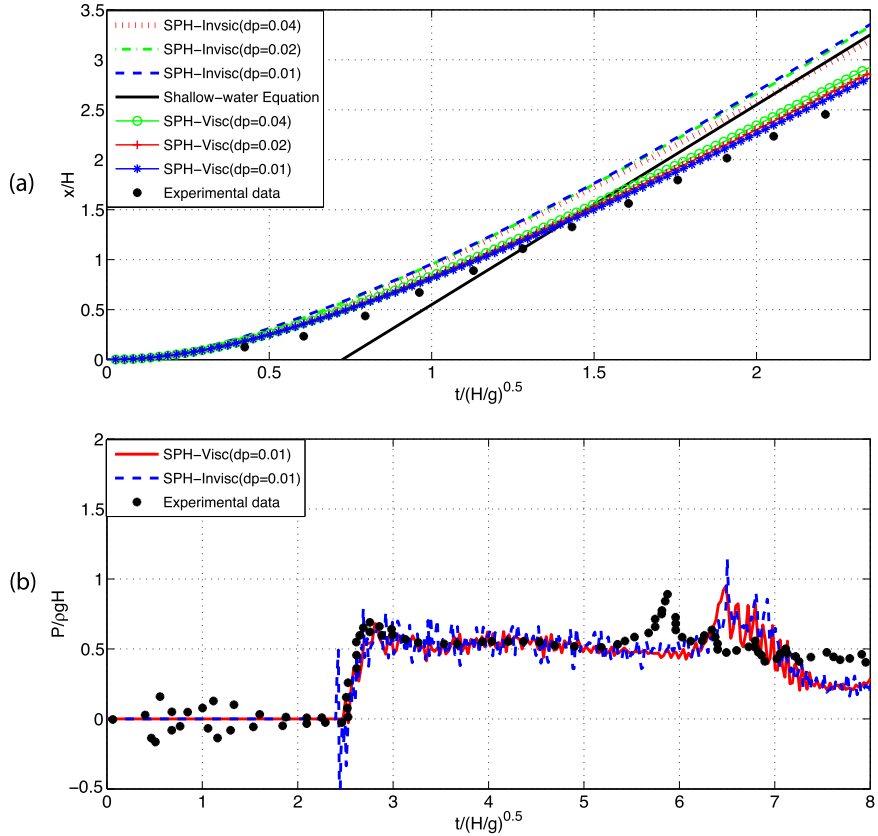


Fig. 15. Results for the dam-break problem: (a) Time evolution of the liquid-front from inviscid and viscous solutions compared with theoretical and experimental data [44]; (b) Comparison of pressure profile between numerical simulations and experimental data [45].

where $b = -8\pi^2/R_e$ is the decay rate of the velocity field, U is the maximum velocity, R_e is the Reynolds number and here we set $R_e = 100$ corresponding to the work of Adami et al. [14].

In this simulation, the computation is performed on a square domain with unit length $L = 1$, and a periodic boundary condition is applied in both coordinate directions. The initial velocity distribution is given by setting $t = 0$ and $U = 1$. The

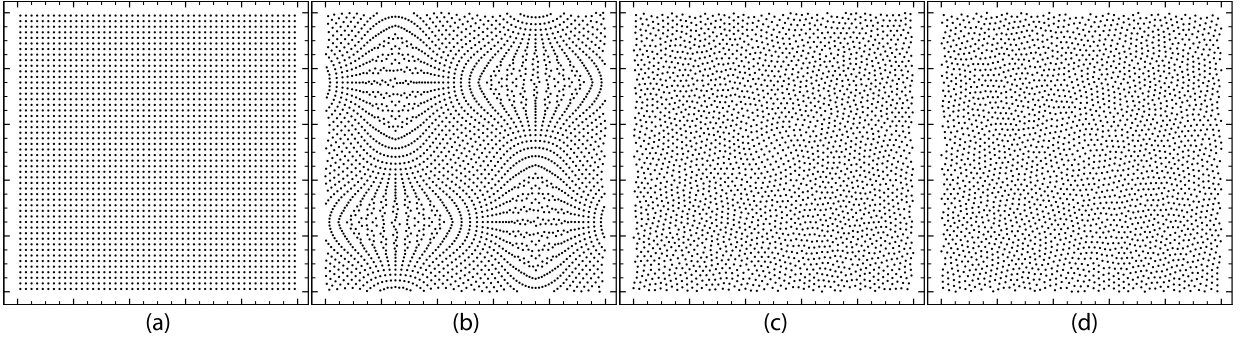


Fig. 16. Particle snapshots for the Taylor–Green problem at $R_e = 100$ with a resolution of 50×50 particles: (a) $t = 0.0$ s, (b) $t = 0.2$ s, (c) $t = 0.4$, (d) $t = 0.8$ s.

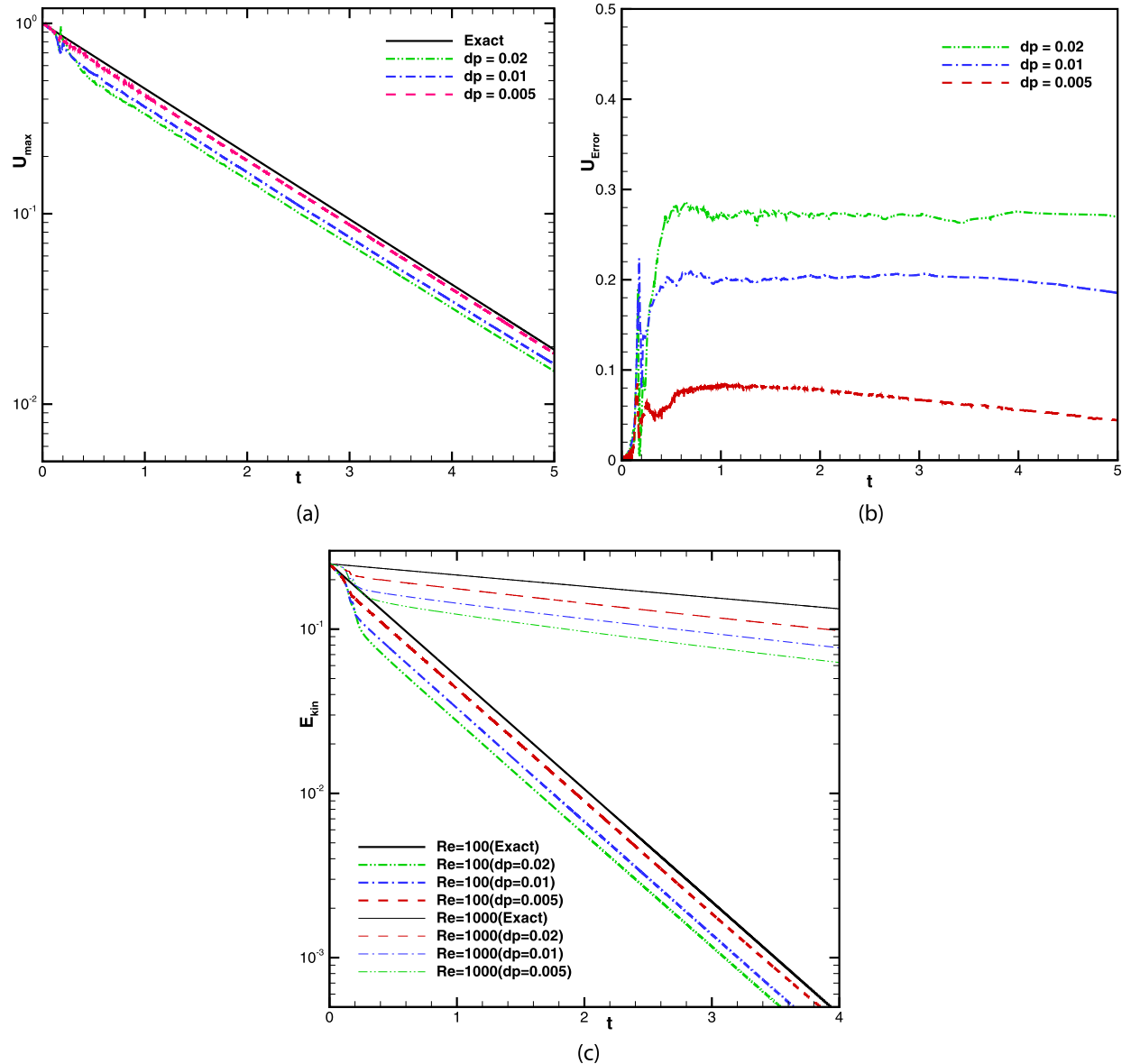


Fig. 17. Numerical results of the Taylor–Green problem: (a) Decay of the maximum velocity ($R_e = 100$); (b) Relative error of the maximum velocity ($R_e = 100$); (c) Decay of the kinetic energy ($R_e = 100$ and $R_e = 1000$).

convergence study is performed by three different resolutions, $\Delta x = 0.02$ (50×50 particles), $\Delta x = 0.01$ (100×100 particles) and $\Delta x = 0.005$ (200×200 particles).

The particle distributions at several time instants with a resolution of 50×50 particles are shown in Fig. 16. It can be observed that a homogeneous particle distribution without clustering is produced. As the simulation starts from a regular lattice particle distribution, particles assume a relaxed configuration at $t = 0.2$ s, as also observed in Adami et al. [14].

Figs. 17 (a) and 17 (c) give the time evolution of the maximum velocity and the total kinetic energy with three resolutions and the analytical solutions. Fig. 17 (b) shows the relative error defined by $L_\infty = \left| \frac{\max(v_i(t) - U_e^{bt})}{U_e^{bt}} \right|$. It can be observed that these results are in quite good agreement with that (see their Fig. 5) obtained by the original transport-velocity formulation [14]. Figs. 17 (c) also gives the evolution of the total kinetic energy for the flow with $Re = 1000$ suggesting correct decay rate with increasing resolution.

5. Conclusions

While many approaches have been proposed to address the well-known tensile instability of the SPH method, none of them is generally effective. In this work, we propose such a method as simple generalization of the previously proposed transport-velocity formulation. The generalization leads to transport-velocity correction which is proportional to the magnitude of the particle pressure, and a restriction of the correction so that it is only affected by the nearest neighbors. By reproducing the simulation of the Taylor–Green vortex, the present method preserves the accuracy of the original transport-velocity formulation. Furthermore, numerical results for a range of fluid and solid dynamics problems show that the present method generally eliminates the tensile instability. Generality and stability of the present method suggest that it has the potential to supersede current standard SPH.

Acknowledgement

The first author is partially supported by China Scholarship Council (No. 2011623002).

References

- [1] L.B. Lucy, A numerical approach to the testing of the fission hypothesis, *Astron. J.* 82 (1977) 1013–1024.
- [2] R.A. Gingold, J.J. Monaghan, Smoothed particle hydrodynamics: theory and application to non-spherical stars, *Mon. Not. R. Astron. Soc.* 181 (3) (1977) 375–389.
- [3] J.W. Swegle, D.L. Hicks, S.W. Attaway, Smoothed particle hydrodynamics stability analysis, *J. Comput. Phys.* 116 (1) (1995) 123–134.
- [4] I. Schuessler, D. Schmitt, Comments on smoothed particle hydrodynamics, *Astron. Astrophys.* 97 (1981) 373–379.
- [5] G.R. Johnson, S.R. Beissel, Normalized smoothing functions for SPH impact computations, *Int. J. Numer. Methods Eng.* 39 (16) (1996) 2725–2741.
- [6] P.W. Randles, L.D. Libersky, Smoothed particle hydrodynamics: some recent improvements and applications, *Comput. Methods Appl. Mech. Eng.* 139 (1) (1996) 375–408.
- [7] D.A. Mandell, C.A. Wingate, L.A. Schwalbe, Computational Brittle Fracture Using Smooth Particle Hydrodynamics, Tech. Rep., Los Alamos National Lab., NM, United States, 1996.
- [8] G.A. Dilts, Moving-least-squares-particle hydrodynamics—I. Consistency and stability, *Int. J. Numer. Methods Eng.* 44 (8) (1999) 1115–1155.
- [9] C.T. Dyka, P.W. Randles, R.P. Ingel, Stress points for tension instability in SPH, *Int. J. Numer. Methods Eng.* 40 (13) (1997) 2325–2341.
- [10] P.W. Randles, L.D. Libersky, Normalized SPH with stress points, *Int. J. Numer. Methods Eng.* 48 (10) (2000) 1445–1462.
- [11] J.P. Gray, J.J. Monaghan, R.P. Swift, SPH elastic dynamics, *Comput. Methods Appl. Mech. Eng.* 190 (49) (2001) 6641–6662.
- [12] J.J. Monaghan, SPH without a tensile instability, *J. Comput. Phys.* 159 (2) (2000) 290–311.
- [13] L. Lobovský, J. Křen, Smoothed particle hydrodynamics modelling of fluids and solids, *Appl. Comput. Mech.* 1 (49) (2007) 521–530.
- [14] S. Adami, X.Y. Hu, N.A. Adams, A transport-velocity formulation for smoothed particle hydrodynamics, *J. Comput. Phys.* 241 (2013) 292–307.
- [15] X.Y. Hu, N.A. Adams, An incompressible multi-phase SPH method, *J. Comput. Phys.* 227 (1) (2007) 264–278.
- [16] X. Hu, N. Adams, A SPH model for incompressible turbulence, *Proc. IUTAM* 18 (2015) 66–75.
- [17] S. Litvinov, X.Y. Hu, N.A. Adams, Towards consistency and convergence of conservative SPH approximations, *J. Comput. Phys.* 301 (2015) 394–401.
- [18] J. Monaghan, On the problem of penetration in particle methods, *J. Comput. Phys.* 82 (1) (1989) 1–15.
- [19] R. Xu, P. Stansby, D. Laurence, Accuracy and stability in incompressible sph (isph) based on the projection method and a new approach, *J. Comput. Phys.* 228 (18) (2009) 6703–6725.
- [20] S. Lind, R. Xu, P. Stansby, B. Rogers, Incompressible smoothed particle hydrodynamics for free-surface flows: a generalised diffusion-based algorithm for stability and validations for impulsive flows and propagating waves, *J. Comput. Phys.* 231 (4) (2012) 1499–1523.
- [21] R. Vacondio, B. Rogers, P. Stansby, P. Mignosa, J. Feldman, Variable resolution for sph: a dynamic particle coalescing and splitting scheme, *Comput. Methods Appl. Mech. Eng.* 256 (2013) 132–148.
- [22] J. Monaghan, A turbulence model for smoothed particle hydrodynamics, *Eur. J. Mech. B, Fluids* 30 (4) (2011) 360–370.
- [23] D.D. Holm, Fluctuation effects on 3d lagrangian mean and eulerian mean fluid motion, *Physica D* 133 (1) (1999) 215–269.
- [24] A. Colagrossi, M. Landrini, Numerical simulation of interfacial flows by smoothed particle hydrodynamics, *J. Comput. Phys.* 191 (2) (2003) 448–475.
- [25] W. Benz, E. Asphaug, Impact simulations with fracture. i. method and tests, *Icarus* 107 (1) (1994) 98–116.
- [26] W. Benz, E. Asphaug, Simulations of brittle solids using smooth particle hydrodynamics, *Comput. Phys. Commun.* 87 (1) (1995) 253–265.
- [27] J.P. Morris, P.J. Fox, Y. Zhu, Modeling low Reynolds number incompressible flows using SPH, *J. Comput. Phys.* 136 (1) (1997) 214–226.
- [28] J.J. Monaghan, Simulating free surface flows with SPH, *J. Comput. Phys.* 110 (2) (1994) 399–406.
- [29] J.J. Monaghan, Smoothed particle hydrodynamics, *Rep. Prog. Phys.* 68 (8) (2005) 1703.
- [30] H. Wendland, Piecewise polynomial, positive definite and compactly supported radial functions of minimal degree, *Adv. Comput. Math.* 4 (1) (1995) 389–396.
- [31] L.D. Landau, E.M. Lifchits, Course of Theoretical Physics: Theory of Elasticity, Butterworth–Heinemann, 1986.
- [32] A.J. Piekutowski, Effects of scale on debris cloud properties, *Int. J. Impact Eng.* 20 (6) (1997) 639–650.

- [33] A.J. Piekutowski, M.J. Forrestal, K.L. Poormon, T.L. Warren, Penetration of 6061-t6511 aluminum targets by ogive-nose steel projectiles with striking velocities between 0.5 and 3.0 km/s, *Int. J. Impact Eng.* 23 (1) (1999) 723–734.
- [34] H.F. Swift, Hypervelocity impact mechanics, in: *Impact Dynamics*, 1982, pp. 215–239.
- [35] J.A. Zukas, *High Velocity Impact Dynamics*, Wiley-Interscience, 1990.
- [36] M.L. Wilkins, Calculation of Elastic-Plastic Flow, Tech. rep., DTIC Document, 1963.
- [37] L.D. Libersky, A.G. Petschek, Smooth particle hydrodynamics with strength of materials, in: *Advances in the Free-Lagrange Method Including Contributions on Adaptive Gridding and the Smooth Particle Hydrodynamics Method*, Springer, 1991, pp. 248–257.
- [38] B. Howell, G. Ball, A free-Lagrange augmented Godunov method for the simulation of elastic-plastic solids, *J. Comput. Phys.* 175 (1) (2002) 128–167.
- [39] V. Mehra, S. Chaturvedi, High velocity impact of metal sphere on thin metallic plates: a comparative smooth particle hydrodynamics study, *J. Comput. Phys.* 212 (1) (2006) 318–337.
- [40] M. Antuono, A. Colagrossi, D. Le Touzé, J. Monaghan, Conservation of circulation in SPH for 2D free-surface flows, *Int. J. Numer. Methods Fluids* 72 (5) (2013) 583–606.
- [41] S. Adami, X. Hu, N. Adams, A generalized wall boundary condition for smoothed particle hydrodynamics, *J. Comput. Phys.* 231 (21) (2012) 7057–7075.
- [42] L. Lobovský, E. Botia-Vera, F. Castellana, J. Mas-Soler, A. Souto-Iglesias, Experimental investigation of dynamic pressure loads during dam break, *J. Fluids Struct.* 48 (2014) 407–434.
- [43] A. Ferrari, M. Dumbser, E.F. Toro, A. Armanini, A new 3d parallel SPH scheme for free surface flows, *Comput. Fluids* 38 (6) (2009) 1203–1217.
- [44] J.C. Martin, W.J. Moyce, Part IV. An experimental study of the collapse of liquid columns on a rigid horizontal plane, *Philos. Trans. R. Soc. Lond. Ser. A, Math. Phys. Sci.* 244 (882) (1952) 312–324.
- [45] B. Buchner, *Green Water on Ship-Type Offshore Structures*, PhD thesis, TU Delft, Delft University of Technology, 2002.
- [46] A. Ritter, Die fortpflanzung de wasserwellen, *Z. Ver. Dtsch. Ing.* 36 (33) (1892) 947–954.
- [47] M. Greco, A two-dimensional study of green-water loading.